ELSEVIER

Journal of Structural Geology 27 (2005) 283–301

JOURNAL OF STRUCTURAL GEOLOGY

www.elsevier.com/locate/jsg

# Shear localisation and strain distribution during tectonic faulting—new insights from granular-flow experiments and high-resolution optical image correlation techniques

J. Adam[a,*], J.L. Urai[b], B. Wieneke[c], O. Oncken[a], K. Pfeiffer[c], N. Kukowski[a], J. Lohrmann[a], S. Hoth[a], W. van der Zee[b], J. Schmatz[b]

[a]*GeoForschungsZentrum Potsdam, Telegrafenberg, D-14473 Potsdam, Germany*
[b]*Endogene Dynamik, Department Georesources and Materials Technology, RWTH Aachen University, Lochnerstrasse 4-20, D-52056 Aachen, Germany*
[c]*LaVision GmbH, Anna-Vandenhoeck-Ring 19, D-37081 Göttingen, Germany*

Received 3 November 2003; accepted 21 July 2004
Available online 21 November 2004

**Abstract**

Brittle faults reflect a complex strain history that emerges from contrasting modes of distributed and localised deformation, and their interaction on various spatial and temporal scales. To better understand this process, we monitor the displacement field in scaled tectonic model experiments using high-resolution optical image correlation techniques (particle imaging velocimetry, PIV).

2D and 3D surface displacement data of extensional and contractional sandbox experiments show that the mode, pattern, and temporal variation of strain accumulation are strongly dependent on the non-linear strain-dependent frictional strength of granular model materials similar to natural deformation processes in brittle rocks. Strain hardening and softening control the shear zone formation.

The pattern of localised deformation is established much earlier than is visible from visual inspection of the experiment. Evolution of distributed strain in the surrounding material of the shear zones and discontinuous shear re-localisation control later stages irrespective of the kinematic boundary conditions.

High-resolution optical strain monitoring quantifies the spatial and temporal patterns of strain accumulation in our model experiments with unprecedented detail. Together with detailed characterisation of the deformation behaviour of the model materials, our experiments will help to re-evaluate important scaling issues, and allow accurate comparison of analogue experiments with numerical simulations.
© 2004 Elsevier Ltd. All rights reserved.

*Keywords:* Analogue experiments; Granular flow; Strain accumulation; Brittle deformation; Displacement field; Shear zone

## 1. Introduction

Scaled sandbox experiments have proven to be an effective tool to simulate brittle deformation processes with high resolution in 2D/3D space (e.g. McClay and Ellis, 1987; Dahlen and Suppe, 1988; Huiqui et al., 1992; Lallemand et al., 1994; Gutscher et al., 1996; McClay, 1996; Wang and Davis, 1996; Koyi, 1997; Kukowski et al., 2002; Lohrmann et al., 2003). They allow observation of the spatial and temporal evolution of brittle deformation structures in laboratory-scaled model systems. The fundamental deformation processes and their controlling parameters can be systematically studied under well-constrained conditions, e.g. varying geometries, material properties, and the magnitude and duration of deformation.

The major advantage of granular materials in model experiments of tectonic faulting is that granular-flow systems show complex non-linear deformation processes with pre-failure distributed deformation, spontaneous shear localization, and dominant strain accumulation in narrow shear zones with significantly reduced strength with respect to the undeformed host material (Marchner and Vermeer, 2001). Comparable deformation processes are characteristic

* Corresponding author. Now at: Department of Earth Sciences, Dalhousie University, Halifax, Nova Scotia, Canada B3J 3J5. Tel.: +1-902-494-3622; fax: +1-902-494-6889
*E-mail address:* j.adam@dal.ca (J. Adam).

0191-8141/$ - see front matter © 2004 Elsevier Ltd. All rights reserved.
doi:10.1016/j.jsg.2004.08.008

for brittle deformation processes in the upper crust (Mandl, 1988; Marone, 1998). Because of this similarity, sandbox models can be used to study the kinematics of tectonic deformation, although some properties such as elastic modulus and width of the shear zone are not scaled. In addition, although in both model and nature the materials show a similar elastic/plastic material behaviour, the full constitutive behaviour is much more complex, involving for example pre-failure strain hardening and post-failure strain softening. Recent studies have shown that these transient properties have an important effect on kinematics in sandbox models of crustal deformation processes (Lohrmann et al., 2003).

Conventional sandbox experiments focus on structural visualization of fault and shear zone kinematics, disregarding the details of the displacement field. This is unfortunate, because with high-resolution analysis of the displacement field sandbox experiments could provide much more information on the complex modes of strain accumulation, their feedback mechanisms and controlling parameters.

At present, the spatial ($\Delta x$) and temporal ($\Delta t$) resolution of strain data are limited by the effort required for the time-consuming standard techniques such as manual digitising of marker points for strain computations. High-resolution displacement measurements are restricted to geotechnical applications, where the deformation of soils and other granular materials is analysed with marker points by photogrammetric techniques.

Recently, displacement monitoring by optical image correlation techniques (PIV: particle imaging velocimetry, commonly used for dynamic flow analysis of fluids and gases in laboratory-scaled systems) was tested to investigate granular deformation processes without the restriction of limited marker points (White et al., 2001; Adam et al., 2002; Wolf et al., 2003).

In this paper we present results of optical image correlation techniques with coupled 2D/3D PIV for high resolution displacement monitoring in sandbox experiments with different boundary conditions and material properties. The 2D and 3D displacement and strain data demonstrate that the complete displacement field can be derived efficiently even from complex experiments by PIV analysis with an enhancement of the spatial and temporal resolution of at least an order of magnitude in comparison with conventional analysis techniques.

This method provides high-resolution measurements of the evolution of patterns of progressive deformation both inside the shear zones and in the surrounding material. It shows how many aspects of the complex displacement field are controlled by the transient material properties of the granular material. In future studies, high-resolution PIV analysis of model experiments of tectonic processes will allow a much better comparison with both numerical models and GPS-based patterns of neotectonic deformation.

## 2. Scales of deformation in sandbox experiments

For conventional strain analysis, the structural information such as displacements of marker layers, marker points, fault geometries and shapes of deforming bodies are digitised from sequential photo or video images with a given spatial and temporal resolution ($\Delta x$, $\Delta t$). The spatial resolution $\Delta x$ is limited by the amount and accuracy of the manually digitised data with a theoretical maximum precision limited to a single pixel of image data. The temporal resolution $\Delta t$ is given by the time interval of analysed images. Because most steps of a strain analysis cannot be done automatically, $\Delta t$ cannot be arbitrarily decreased. With higher resolution the time expense for data acquisition increases drastically.

Generally, strain data derived from sandbox experiments with a focus on structural evolution are characterised by a maximum spatial resolution at the millimetre-scale ($\Delta x \geqq 1$ mm) and a temporal resolution up to several seconds ($\Delta t \geqq 10$ s) depending on size and duration of the experiment and its strain rate ('structural evolution' in Fig. 1).

Quantitative analysis of small-scale distributed deformation (strain localisation in Fig. 1: 0.1 mm (or grain size) $\leq \Delta x \leq 10$ mm, 1 s $\leq \Delta t \leq 10^3$ s), surface deformation processes as well as surface mass movements (surface processes in Fig. 1: 1 mm $\leq \Delta x \leq 10^3$ mm, 1 s $\leq \Delta t \leq 10^2$ s), and velocity-dependent unstable deformation processes (stick-slip deformation in Fig. 1: 0.1 mm $\leq \Delta x \leq 10$ mm, 0.1 s $\leq \Delta t \leq 10$ s) requires an increased spatial and/or temporal resolution of at least an order of magnitude in comparison with conventional analysis used in sandbox experiments with scaling factors of $10^5$–$10^6$. More precise displacement measurements in sandbox experiments can be

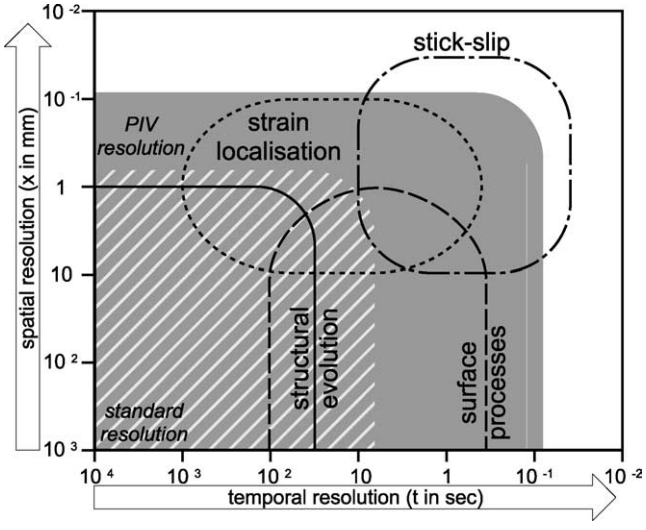


Fig. 1. Synoptical diagram illustrating the spatial and temporal range of deformation processes in laboratory-scaled granular-flow experiments and the resolution of strain data obtained by standard image analysis (standard resolution, hatched area) and optical image correlation (PIV resolution, shaded area).

achieved by comparing time-lapse image sequences using stereoscopic techniques (Horsefield, 1977; Mandl, 1988, 2000). This method also is time-consuming but allows the construction of contour diagrams of displacement rate with much higher spatial resolution ($\Delta x < 1$ mm).

## 3. Methods

### 3.1. 2D strain monitoring by PIV

Particle imaging velocimetry (PIV) provides an accurate measure of the instantaneous velocity/displacement field of laboratory flow and deformation systems and is adapted in this study for high-resolution 2D/3D strain monitoring in analogue sandbox experiments. PIV is an optical, non-intrusive method for non-linear flow and deformation visualisation by optical image correlation techniques. In granular-flow experiments, optical image correlation enables spatial resolution of the displacement data in the range of the particle size of the sand material (White et al., 2001). The temporal resolution is only limited by the computer hardware (camera frame rate, data transfer rate and storage capacity) due to the automated analysis. Thus, PIV data cover the complete range of structural evolution, strain localisation and surface processes, as well as a major part of the stick-slip field in experiments that scale by a factor of $10^5$–$10^6$ (see Fig. 1).

2D deformation in sandbox experiments is recorded by sequential digital images The corresponding displacement field is computed by cross-correlation from the translation and distortion of the sand particle pattern in successive images with given time interval *dt* (Fig. 2A). The basic steps of cross-correlation and computation of the 2D displacement field are explained in detail in Appendix A.

Local displacement vectors are calculated for small sub-samples (*n*, *m*) of the images (interrogation window, Fig. 2B). The digital cross-correlation of the particle pattern yields a spatial average of the local displacement vector over the size of the sub-sample (Fig. 2C). The complete displacement field consists of the vectors (*n*, *m*) of all sub-samples (Fig. 2D). A higher validation rate and spatial resolution is reached by adaptive multi-pass correlation (Fincham and Spedding, 1997; Scarano and Riethmuller, 2000; Wieneke, 2001) and a step-wise decreasing sub-sample size (Fig. 2E), which allows the detection of large deformations and the measurement of strong displacement gradients with high spatial resolution.

The incremental displacement vector field forms the basis for further calculations of the local displacement components or derived values such as the strain tensor components and the corresponding strain rates. Further values can be derived from these scalar fields, for example, the incremental shear strain $E_{xy}$ and the incremental rotational shear *rot-z*. These are very useful to monitor strain accumulation and shear zone formation in the experiments. While these incremental displacement and strain data monitor the spatial and temporal variation of the deformation in the experiments, time-series analysis of the incremental displacement and strain data provides information on the total displacement field and the finite strain.

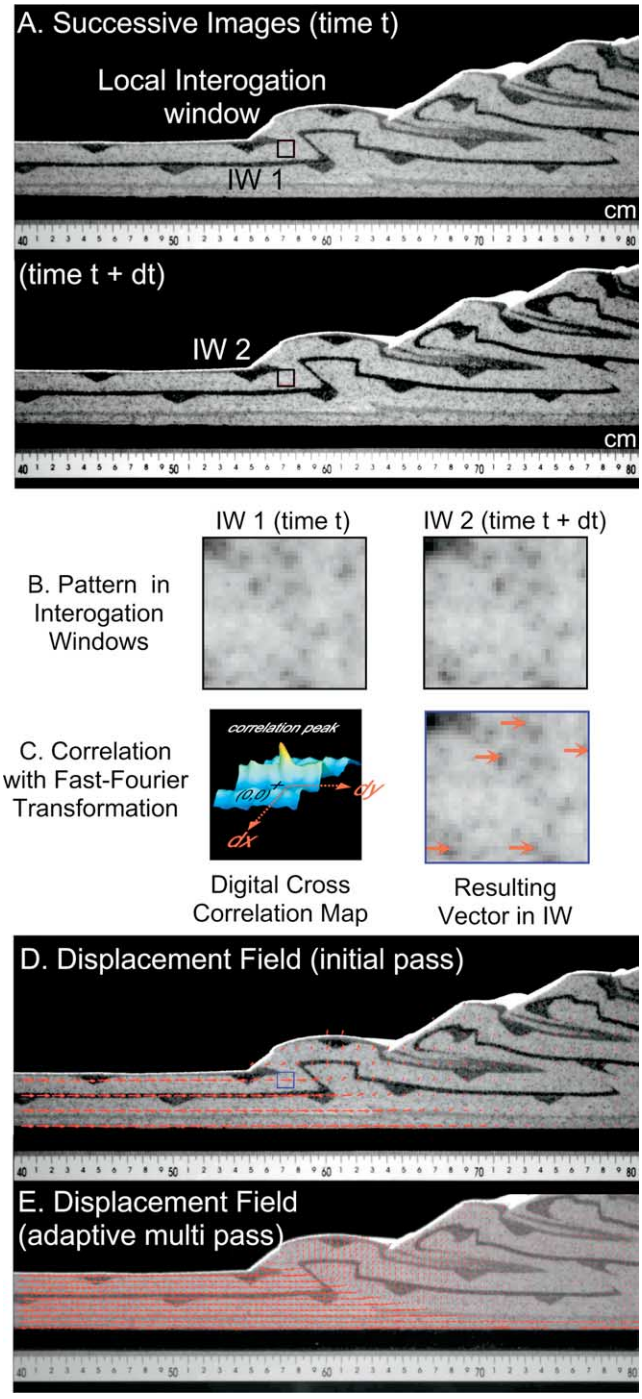


Fig. 2. Computation of the 2D displacement field in contractional dry sandbox experiment by optical image correlation: (A) successive digital images with sub-samples (interrogation window, IW 1, IW 2), (B) particle pattern in sub-samples with local shift, (C) calculation of the local displacement vector (*dx*, *dy*) by cross-correlation (correlation peak), (D) complete displacement field from single pass correlation, (E) final displacement field from adaptive multi-pass cross-correlation.

### 3.2. 3D surface deformation monitoring by stereo PIV

In sandbox experiments the main application of 3D PIV is the measurement of the surface response to internal deformation and to monitor surface mass transport. In the experiments the 3D deformation of the model surface is monitored by a stereoscopic camera setup (Fig. 3) and is analysed by 3D PIV correlation of the sequential stereo images (Fig. 4a).

In contrast to 2D correlation, the 3D procedure consists of three successive steps. At first, a 3D volume calibration for the given experimental volume must be performed to provide a mapping function $M'$ for image correction. For each pair of stereo images the following static surface height calculation with $M'$ provides a scalar field describing the actual surface of the object that is a prerequisite for 3D displacement calculation (Fig. 4b). With the surface height information and the mapping function $M'$, the 3D displacement field is measured by cross-correlation from successive stereo images similar to 2D PIV. The resulting 3D vector field describes the spatial displacement of every surface element (Fig. 4d, refer to Appendix B for further information).

### 3.3. Precision of PIV correlation

The absolute spatial resolution ($dx$) of the displacement field data depends on the optical resolution of the digital camera system and the precision of the cross-correlation algorithm (refer to Appendix C for detailed discussion).

Image data from digital cameras of the consumer segment are suitable for PIV analysis (used for the extensional wet sandbox experiment shown in Fig. 11) but have some limitations that influence the outcome of the correlation algorithm and hence lower the PIV correlation accuracy. The effective spatial resolution is reduced by conversion from colour to monochrome scalar intensities and some information loss is caused by the implemented image compression algorithm.

For experiments that require higher resolutions, digital monochrome CCD cameras (charge-coupled device) which are optimised for PIV monitoring allow image acquisition with high optical resolution and without loss of intensity information by image conversion and compression (used for the contractional dry sandbox experiment).

Besides these camera properties, the PIV correlation algorithm controls the displacement vector accuracy. As demonstrated by White et al. (2001), PIV correlation allows the calculation of displacement vectors with sub-pixel accuracy ($<0.1$ pixel). For the adaptive multi-pass cross correlation algorithm (StrainMaster©, LaVision GmbH, 2002), used in this study, the accuracy of the vectors is on average significantly smaller than 0.1 pixel and ranges from 0.03 to 0.2 pixel depending on the sub-sample size and

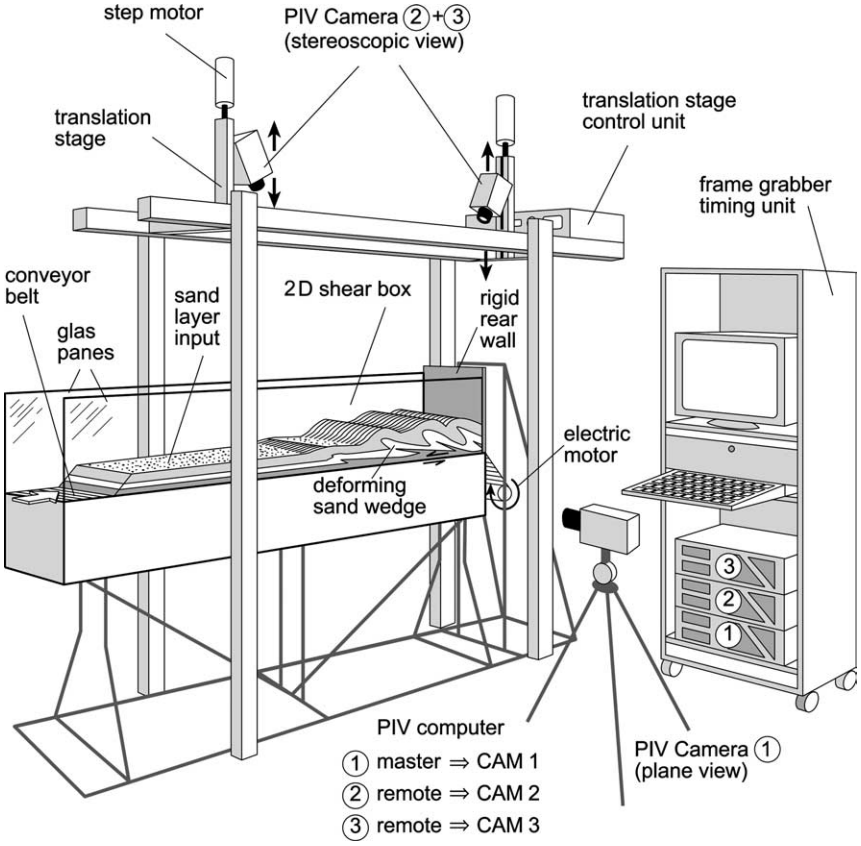


Fig. 3. Experimental setup for 2D/3D PIV monitoring in contractional sandbox experiments. Stereo cameras for 3D surface monitoring are mounted on translation stages to allow vertical adjustment and 3D volume calibration.

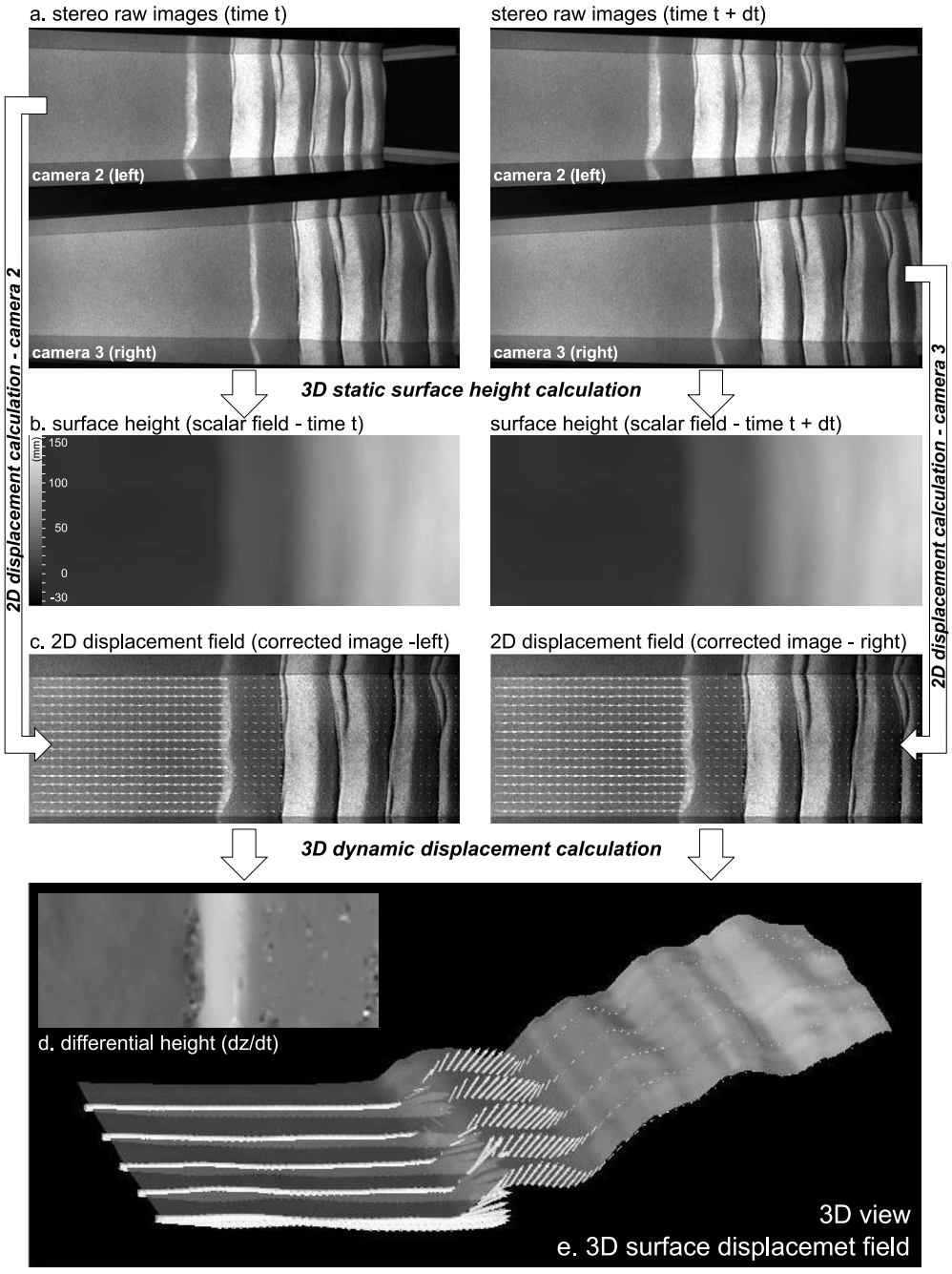


Fig. 4. 3D surface displacement calculated by cross-correlation from successive stereo images: (a) stereo images of wedge surface at time ($t$), ($t+dt$), (b) calculated scalar field of surface height, (c) 2D displacement field calculated from corrected images, (d) surface height variation ($dz/dt$), (e) 3D wedge surface with displacement vectors.

image contrast (LaVision, 2002). With a given optical vector accuracy of better than 0.1 pixel, the absolute accuracy of the displacement vectors depends on image scaling and correction. For example, with an optical resolution of 4 mega-pixels ($2k\times2k$) and an experiment with 100 cm width, the absolute accuracy of the length of displacement vectors is about 0.05–0.1 mm.

The temporal resolution $dt$ is limited by the frame transfer rate of the digital cameras. Standard digital still cameras provide frame transfer rates of $\sim$0.1 Hz with image compression. Actual digital CCD cameras with 4 mega-pixels resolution adapted for PIV monitoring achieve frame transfer rates of maximum 15 Hz without image compression and no loss of image information.

## 4. 2D–3D PIV analysis of a contractional dry sandbox experiment

To demonstrate the interpretation capabilities of the

2D/3D displacement field data, we present a dry sandbox experiment that simulates brittle deformation processes in an accretionary wedge or fold-and-thrust belt. The experimental device consists of a glass-sided 2D shear box of 200 cm length and 20 cm width. Convergence is simulated by a conveyor belt topped with sand paper (potential basal detachment) that is pulled towards the rigid rear wall by an electric DC motor with a nearly constant velocity ($\sim$10 cm/min).

To study the interaction of subsurface deformation and the surface response, the camera setup is designed for simultaneous monitoring of the 2D deformation in cross-sectional view and corresponding 3D surface deformation in sandbox experiments (Fig. 3). The monitoring system itself consists of three monochrome CCD cameras (LaVision Flowmaster 2S©, 4 mega-pixel, 12 bit) and the PIV recording unit. 2D internal deformation is imaged by one camera in plane view (camera 1 in Fig. 3). 3D surface deformation is recorded simultaneously from above by two cameras in a stereoscopic setup (cameras 2+3 in Fig. 3).

The basal conveyor belt consisting of sandpaper is characterised by substantial roughness and a friction coefficient similar to the sand material. The input layer with a thickness of about 3.5 cm was made of sifted sand with homogeneous mechanical properties. The physical properties of the sand and the basal interface are listed in Table 1. Passive markers with the same mechanical properties as the sifted sand are incorporated only for visualisation and are not required for PIV analysis. During the experimental run, the sand layer was transported on top of the conveyor belt and was deformed in front of the rear wall. The incoming sand layer was successively detached from the basal interface and formed an imbricate thrust wedge (Fig. 5A). In contrast to contractional sand wedges with low basal friction (smooth foil or PVC base material) that are characterised by short thrust segments, a low taper wedge geometry and wedge growth by frontal accretion, this type of a convergent sand wedge with high basal friction is characterised by long thrust segments, large wedge tapers and a growth mode dominated by frontal or basal underplating (Huiqui et al., 1992; Gutscher et al., 1998; Nieuwland et al., 2000a). Technical details of the experiment are summarised in Table 2.

Table 1
Physical properties of analogue materials used in the contractional sandbox experiment based on dynamic measurements with a ring shear tester. For the coefficient of friction, standard error of all measurements was smaller than 1%. The cohesion can only be determined with an accuracy of 5–20 Pa in these measurements performing vertical stresses up to 6000 Pa

| Material | Sand | Sandpaper |
|---|---|---|
| Type | Internal | Basal |
| Grain size | 20–630 μm | 20–400 μm |
| Preparation | Sifted | Relative to sifted sand |
| Density (g/m$^3$) | 1.732±0.008 | – |
| $\mu_{peak}$ | 0.731±0.006 | 0.718±0.031 |
| $C_{peak}$ (Pa) | 63.5±19.8 | – |
| $\mu_{static}$ | 0.601±0.002 | 0.590±0.003 |
| $C_{static}$ (Pa) | 89.6±7.4 | 60.3±8.5 |
| $\mu_{dynamic}$ | 0.568±0.002 | 0.558±0.003 |
| $C_{dynamic}$ (Pa) | 66.5±5.0 | 43.9±10.3 |

### 4.1. 2D-PIV displacement field and interpretation

The incremental and total displacement data provide the complete strain history of the experiment. Fig. 6a shows the incremental displacement vector field ($\Delta t$=1 s, $\Delta x$=2 mm) of the frontal sand wedge at a convergence of 60 cm. Additionally, the displacement magnitude is displayed in the respective background colour map (Fig. 6b). The input

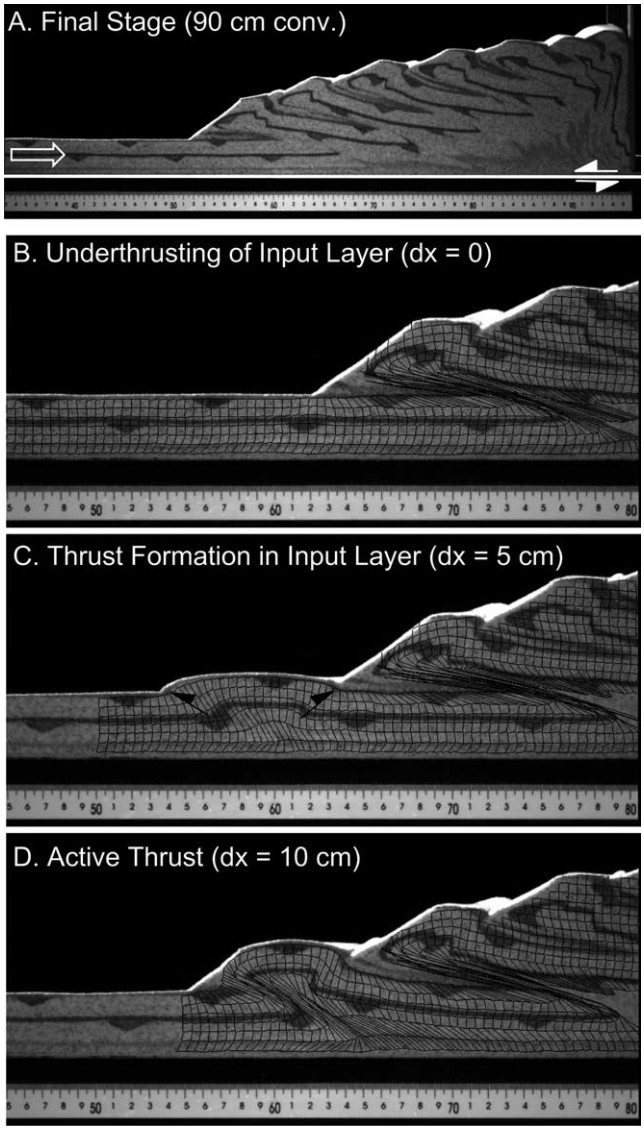


Fig. 5. 2D total deformation in a convergent sand wedge. (A) Final deformation stage after 90 cm of convergence (raw image). (B) to (D) Deformed sand wedge from 53 to 63 cm of convergence. (B) Underthrusting ($dx$=0). (C) Fore- and backthrust formation in input layer ($dx$=5 cm). (D) Active thrust ($dx$=10 cm) with strain localisation in the frontal shear zone and additional homogeneous deformation at the base of the frontal thrust segment.

Table 2
Specifics and database of the contractional dry sandbox experiment

| Dry contractional sandbox experiment (2D/3D PIV) | |
|---|---|
| Scaling factor | $10^5$, 1 cm in model = 1 km in nature |
| Initial setup | Horizontal layer of sifted sand, 3.5 cm thick |
| Sand | 0.02–0.63 mm |
| Basal interface | Sandpaper, high friction and roughness |
| Total convergence | ~140 cm |
| Convergence rate | ~9.6 cm/min |
| Duration | ~13 min |
| PIV frame rate | 1 Hz, $dt = 1$ s |
| PIV raw data | ~800 triple images |

layer is imaged by horizontal vectors with a maximum displacement rate of about 2.0 mm/s that equals the convergence rate of the basal interface (Fig. 6a–c). The deforming sand wedge is characterised by significantly slower displacement rates (0–1 mm/s) and is underlain by a continuous active basal shear zone with intermediate displacement rates (~1.5 mm/s).

At the deformation front, marked by the frontal shear zone, sand particles strongly decelerate. While the transport direction remains horizontal in the basal shear zone, displacement vectors in the frontal shear zone rotate counter-clockwise with active shear top to the left caused by the overthrusting hanging wall sand segment. Wedge-internal displacement is concentrated at the frontal part of the sand wedge overlying the ramp segment. The horizontal ($dx$) and vertical ($dy$) componentS of the displacement field display the contrasting distribution of the convergence and uplift-related displacement (Fig. 6c and d). Deformation in the sand wedge is concentrated in the hanging wall of the frontal shear zone and is dominated by uplift (maximum uplift rate = 0.6 mm/sec). Horizontal displacement focuses in the frontal thrust segments.

From the incremental displacement field, the body distortion, incremental horizontal strain $E_{xx}$, shear strain $E_{xy}$ and flow lines were calculated (see Fig. 6e–h). The incremental body distortion is shown as a deformed vector grid similar to a deformed grid from finite element modelling (Fig. 6e). The grid distortion clearly shows the frontal and basal shear zones.

Additionally, strain localisation and active shear deformation is visualised by the incremental strain tensor components (for example $E_{xx}$ and $E_{xy}$; Fig. 6f and g). For the given time increment ($\Delta t = 1$ s), the incremental strain components correspond to the respective strain rates. Flow lines (Fig. 6h) visualise the actual particle flow and enable the identification of spatial mass flow pattern in the experiment.

From the incremental displacement field data the total strain in the deforming sand material is derived. For each time step ($n$), the vector sum is calculated by Lagrangian summation of the previous incremental displacements ($v(0)+v(1)+\ldots v(n)$). Progressive distortion in the input sand layer and in the frontal wedge is visualised by vector grid deformation for a convergence interval of 10 cm in Fig. 5B–D.

During underthrusting of the undeformed sand layer (Fig. 5B; $dx = 0$), strain was dominantly accumulated in the frontal shear zone and subsequently in the overriding wedge. With ongoing convergence, a new set of conjugate shear zones was initiated in the input layer in front of the sand wedge and an asymmetric frontal pop-up structure evolves (Fig. 5C). Further convergence led to increased strain localisation in the forethrust shear zone (Fig. 5D). Here, the strongly distorted grid cells show the cumulative shear deformation that was accumulated in the frontal shear zone with a width of about 1.0 cm. In addition, a large distributed strain was accumulated in the basal part of the frontal shear zone near the transition from the thrust segment to the basal shear zone.

### 4.2. Strain cycles during shear zone formation

Initial shear zone formation in front of the propagating sand wedge illustrates the complex interaction of different deformation mechanisms during shear localisation The strain history is shown as a time-series of incremental ($dt = 1$ s) and total shear strain data for a convergence interval of about 22 mm (see Fig. 7).

Prior to a new cycle of shear zone formation, the frontal sand wedge was overthrust along the active frontal shear zone on top of the input layer. Shear zone formation was initiated by simultaneous propagation of basal shear strain and minor distributed deformation in the underthrust input layer (total shear strain, $dx = 10.8$ mm; Fig. 7A).

Simultaneous with basal failure beneath the input layer, distributed shear strain was accumulated in front and above the blind tip of the propagating basal shear zone, and the shear strain rate on the former frontal thrust decreased significantly. In front of the sand wedge, total shear strain was subsequently accumulated in a more than 15-cm-broad segment of the input layer (incremental and total shear strain, $dx = 14.4$ mm; Fig. 7B).

With spontaneous shear localisation in conjugate shear zones, the zone of active distributed shear deformation was narrowed significantly and was restricted to the triangular shaped pop-up of 10 cm width in front of the sand wedge ($dx = 18.0$ mm; Fig. 7C). Shear deformation in the pre-existing frontal shear zone ceased. Ongoing convergence led to asymmetric strain accumulation with increasing strain along the kinematically preferred fore-shear zone and decreasing strain along the back-shear zone and a continuously active frontal and basal shear zone with ramp-flat geometry was created ($dx = 21.6$ mm; Fig. 7D).

To map the strain localisation process, the temporal gradient of total strain in the input layer is plotted for 10 displacement increments ($dx = 1.8$ mm) during shear zone formation along a horizontal profile line located 1 cm below the input layer surface (Fig. 8). In the initial phase the shear strain was mainly stored in the frontal thrust ($E_{xy} \sim 0.8$). In

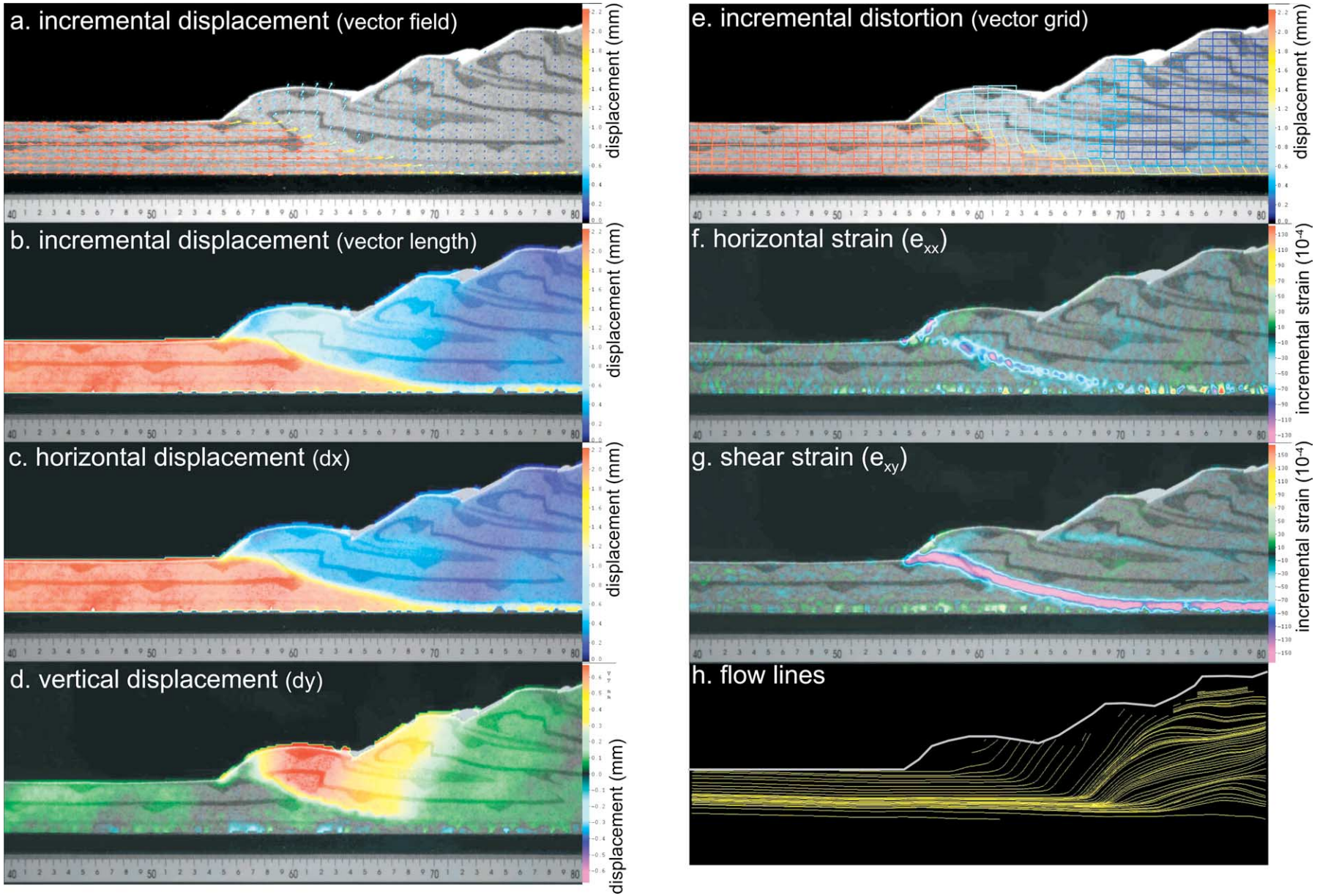


Fig. 6. Incremental 2D-displacement field of convergent sand wedge at 60 cm of convergence for a time interval $dt = 1$ s and deduced displacement and strain components. Displacement field consists of 88000 local vectors with a final grid size of 16 pixels, only every 8th vector in the $x$ and every 4th vector in the $y$ direction is shown: (a) displacement vectors (identical to Fig. 2e), (b) incremental displacement (vector length), (c) horizontal displacement component ($dx$), (d) vertical displacement component ($dy$), (e) body distortion visualised by vector grid deformation, (f) incremental horizontal strain ($E_{xx}$), (g) shear strain ($E_{xy}$), and (h) visualisation of particle displacement by flow lines for the identification of mass flow pattern.

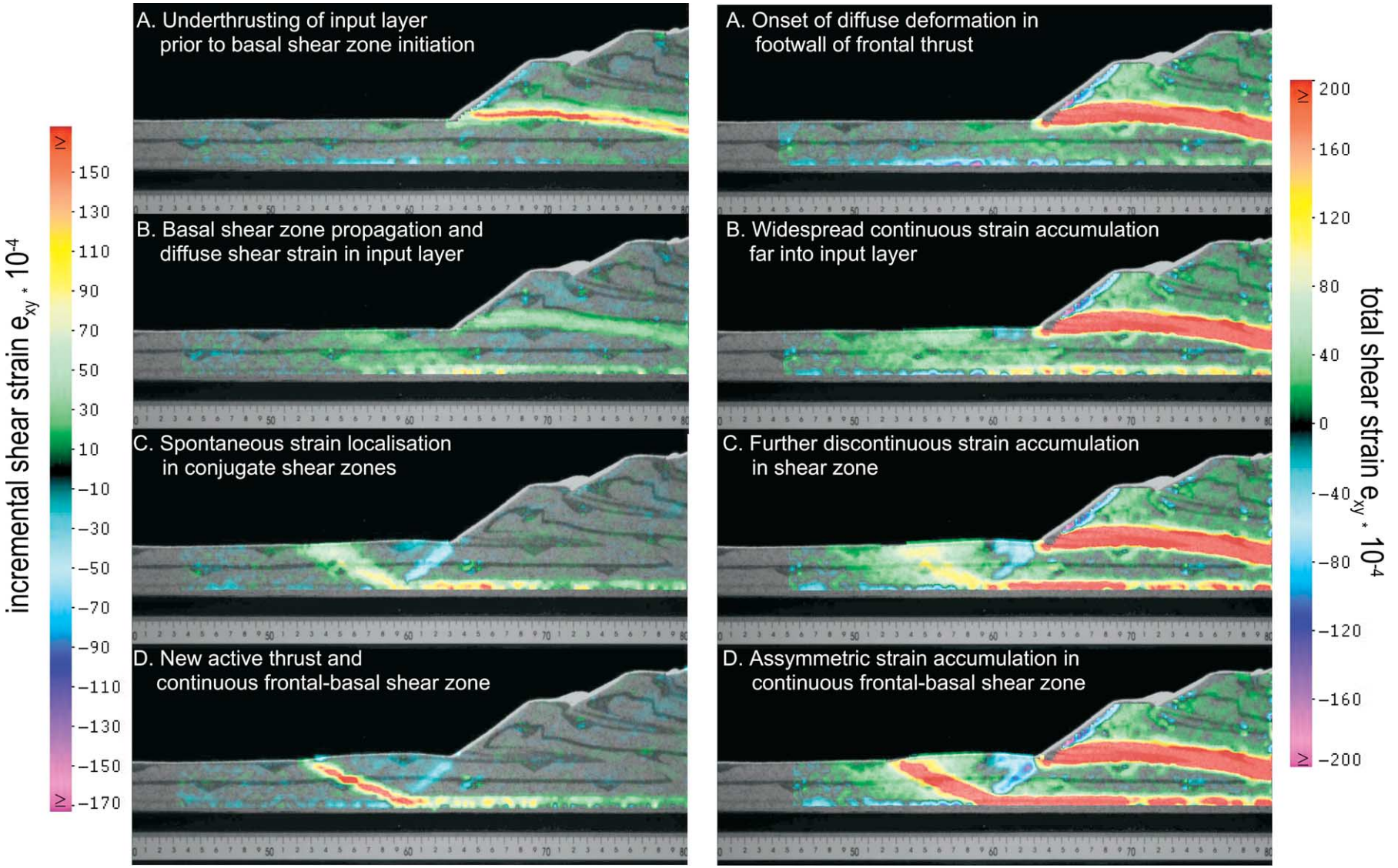


Fig. 7. Time-series data of incremental (left) and total strain accumulation (right) during shear zone formation. (A)–(D) Characteristic evolution stages during 2.2 cm of convergence. (A) Underthrusting of input layer and onset of distributed deformation beneath frontal wedge ($dx = 10.8$ mm). (B) Basal shear zone propagation and distributed strain accumulation in input layer ($dx = 14.4$ mm). (C) Spontaneous strain localisation in conjugate shear zones ($dx = 18.0$ mm). (D) Asymmetric strain accumulation on new active frontal thrust ($dx = 21.6$ mm).

the following steps distributed strain was continuously accumulated in the input layer ($0.02 < |E_{xy}| < 0.1$). This process started in the inner part of the input layer and was growing in an external direction until a more than 150-mm-wide segment of the input layer was stepwise strained (Fig. 8A and B). The inner part developed with opposite shear sense.

Spontaneous strain localisation was initiated in the narrowing forward-directed shear and backward-directed shear domains after a characteristic critical shear strain ($|E_{xy}| \sim 0.1$) was accumulated (Fig. 8C). During strain localisation, these shear zones were narrowed drastically and the shear strain rate increased continuously until shear rates became constant ($\dot{E}_{xy} \approx 0.13\ s^{-1}$ in forward-directed shear zone (equal to $E_{xy}$ at 1 Hz frame rate; Fig. 8D)).

This complex pattern of strain accumulation during initial shear zone formation is governed by the strain-dependent deformation mechanism in the granular matter. Here, pre-failure distributed strain accumulation causes strain hardening. After the material's peak strength is exceeded, strain localisation leads to post-failure strain softening. Strain hardening and softening are accompanied by a compaction–decompaction cycle of the material, which controls the evolution of the frictional strength during progressive deformation as shown in the stress–strain curve of the sand material (S30T) (Fig. 9).

The total shear strain data $E_{xy}$ of the incremental displacement stages of Fig. 8 are scaled to the stress–strain curve to show the relevant deformation mechanism during shear zone formation (circles in Fig. 9). In the previously undeformed input layer the sand material is initially compacted by distributed deformation (A in Fig. 9). In the following stages, increasing distributed deformation indicates the onset of distributed shear and material decompaction in the input layer. This caused widespread strain hardening in the input layer and subsequently established material peak strength (B in Fig. 9).

After exceeding the material's peak strength, spontaneous strain localisation leads to initial shear failure and post-failure strain softening of the previously hardened sand material (C in Fig. 9) characterised by a maximum decompaction rate. With the decay of strain-softening and material decompaction, the constant shear strain rate ($\dot{E}_{xy} \approx 0.13\ s^{-1}$) indicates stable shear and stable strength conditions in the forward-directed shear zone (D in Fig. 9). Stable strength of this active shear zone is significantly lower than peak strength due to strain-softening and enables further deformation within the localised shear zone.

### 4.3. 3D surface deformation of convergent sand wedge

To image the coupled subsurface and surface deformation processes, the 3D displacement vector field that describes the corresponding surface evolution of the same experiment is shown in Fig. 10.

The converging horizontal input layer is imaged by vectors with maximum incremental displacement ($dx =$ 1.8 mm) pointing in the convergence direction (Fig. 10a, 3D view). The morphological features of the sand wedge are characterised by a steep frontal slope at the angle of repose and adjacent a more shallowly inclined surface with a depression-and-ridge topography generated by the previously stacked thrust segments. Upward-directed vectors pointing to the rear wall indicate wedge growth and compressional uplift. 'Slow' sand avalanches along the frontal slope are indicated by down-slope directed displacement vectors that point opposite to the convergence direction. 'Fast' avalanches which were frequently observed in the experiment cannot be imaged because the strong variation of the sand particle pattern along the slope does not allow pattern correlation with the given frame rate of 1 Hz. Only a significantly higher frame rate ($\geqq 5$ Hz) would enable monitoring of the complete sliding activity along the

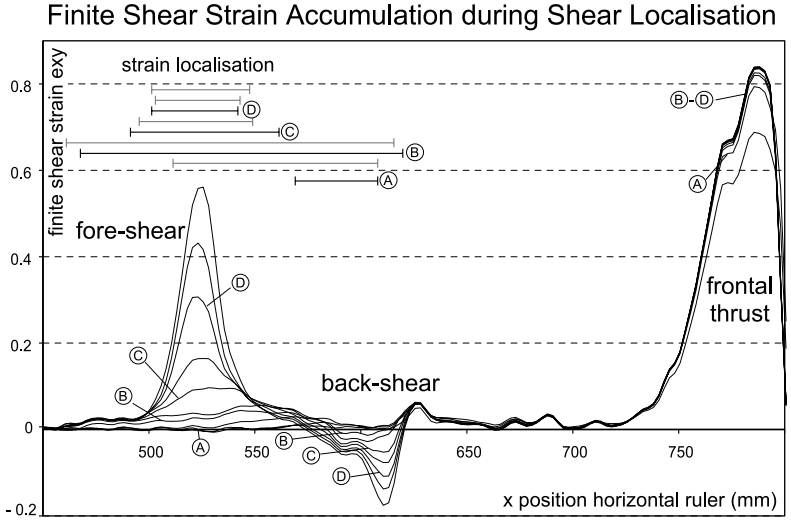


Fig. 8. Shear strain accumulation ($E_{xy}$) and strain localisation during initial shear zone formation (example horizontal profile line 1 cm below input layer surface). Letters A–D indicate the respective deformation stages in the 2D contractional experiment (Fig. 7).

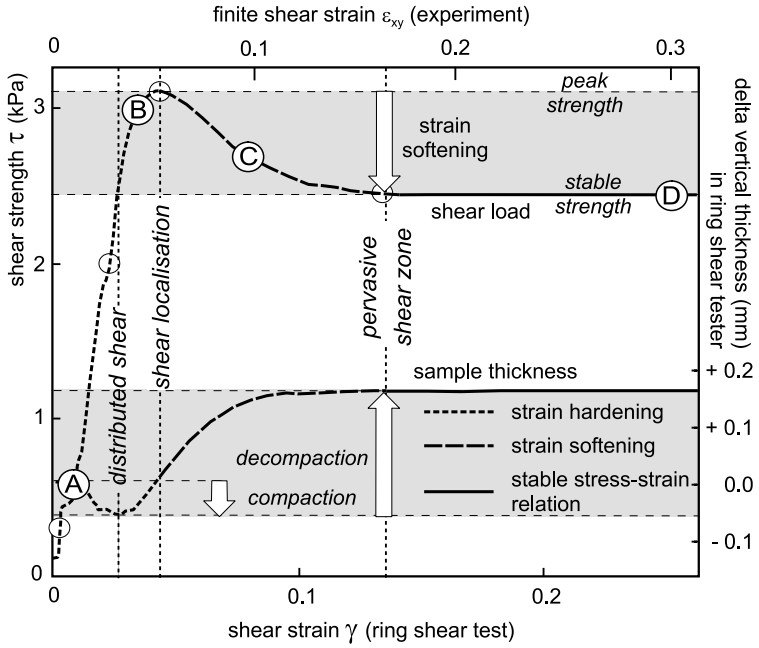


Fig. 9. Characteristic variation of shear load and sample thickness during shear zone formation in sifted sand used in the contractional experiment (derived from dynamic ring shear tests, normal load = 5.27 kPa). Circles and letters indicate scaled profile data of maximum total shear strain $E_{xy}$ during fore-shear zone formation; small circles indicate intermediate profile data (Fig. 8).

frontal slope. Phases with avalanches alternate with stable thrusting phases (Fig. 10b). The spatial distribution of surface uplift and down-slope particle displacement is shown by the incremental vertical displacement component *dz* (Fig. 10a and b, 2D view).

Thrust shear zone formation in front of the propagating sand wedge nucleated surface deformation processes. The rising frontal thrust ridge was characterised by significantly smaller and upward directed displacement vectors in comparison with the incoming layer (Fig. 10c). The thrust ridge was uplifted asymmetrically with maximum uplift above the tip of the propagating basal shear zone as shown by the vertical displacement gradient *dz*. At the same time deformation of the rear part of the sand wedge surface was ceasing, indicating the temporal strain localisation on the new thrust as already observed in 2D view.

Furthermore, continuous thrusting was generating a new ridge that occurred in front of the frontal slope (Fig. 10d). Attributed to successive underthrusting of the new thrust segment, the uplift of the frontal wedge surface successively increased to maximum values as described for the stable thrusting stages.

## 5. 2D extensional wet sandbox experiment

Time-series displacement field data of evolving shear zones in granular-flow experiments are essential to study the kinematic evolution and strain history of fault structures. Even in 'simple' fault structures, when observed at outcrop scale, the discontinuous strain propagation and strain partitioning leads to a rather complex strain history with large strain gradients. To visualise strain propagation and strain partitioning in an evolving fault structure, we present incremental 2D displacement field data of a wet sandbox experiment simulating a basement-controlled normal fault zone that propagates into the overlaying sedimentary rock sequence (Fig. 11). This 2D extensional wet sandbox experiment consists of homogeneous, water-saturated sand to model a simple basement-controlled normal fault structure (van der Zee, 2002; Schmatz et al., 2003; van der Zee et al., 2003).

The experimental device consists of a water tank into which a sandbox is immersed (Fig. 11A). This sandbox consists of two metal blocks sandwiched between parallel glass plates, which represent the rigid basement at the base of the sedimentary sequence. The base of the blocks is permeable to allow equilibration of the water level during the experiment. The moving basement block forms the hanging wall segment of a basement fault and is displaced by a drive shaft attached to a motor outside the water tank. The displacement rate was chosen sufficiently slowly to allow equilibrium of fluid pressure in the sand. The sand is sedimented in the box, which already contains water, to ensure full saturation and a cohesionless material. This results in a higher porosity than in the dry experiments, and almost no softening after peak stress is reached. Therefore, less sharp deformation bands are expected to develop compared with the densely sifted sand as used in the contractional sandbox experiment. For 2D strain analysis, the experiment was recorded with a computer-controlled consumer still digital camera. Technical details of the experiment are summarised in Table 3.

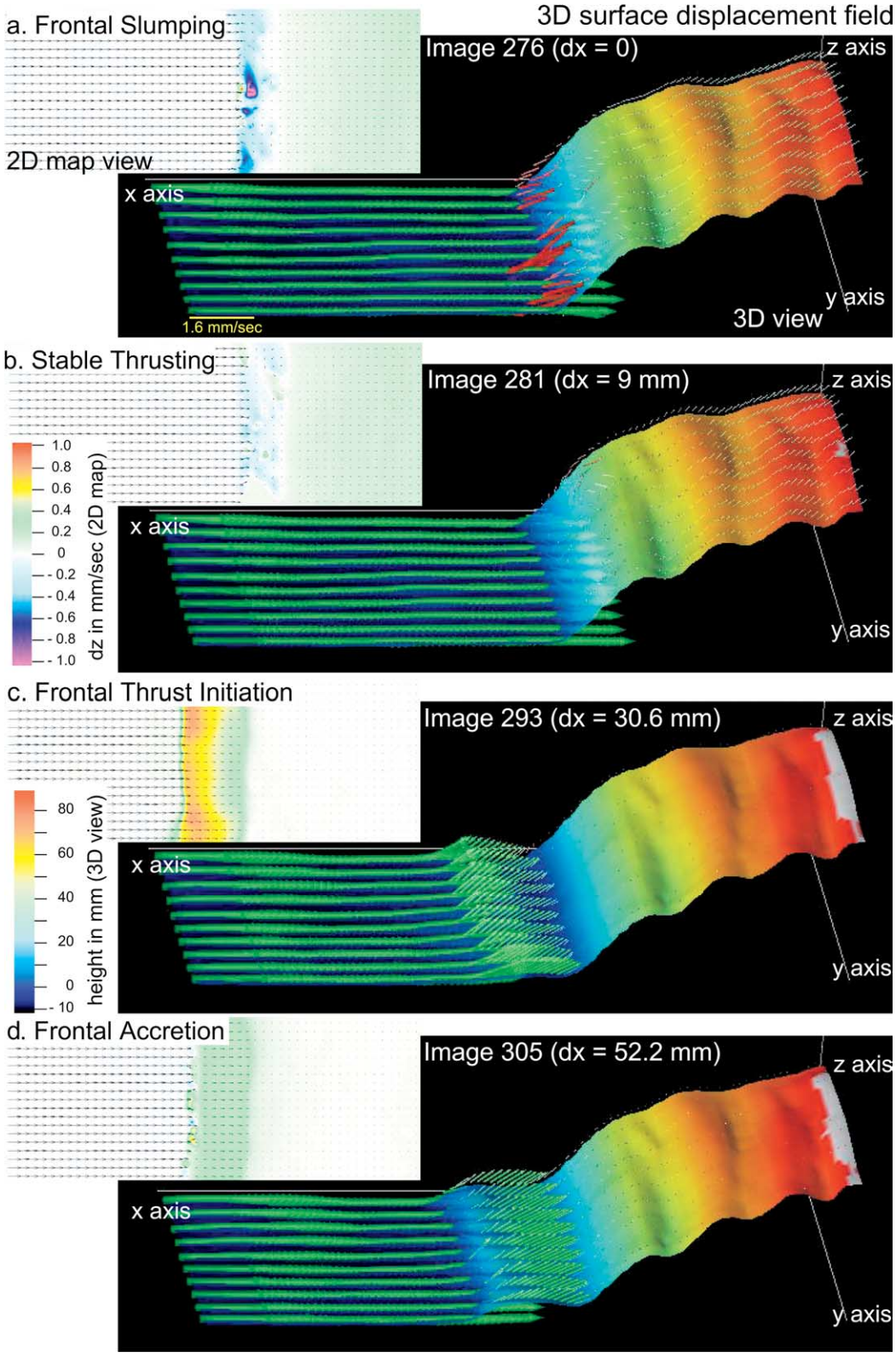


Fig. 10. 3D wedge surface with incremental 3D displacement field of surface elements of the contractional dry sandbox experiment. 3D displacement vectors consist of 16,000 local vectors with a final grid size of 16 pixels; only every 4th vector in the *x* and *y* directions are shown. 2D inset map shows the incremental vertical displacement component *dz*. (a) Propagating wedge with sand avalanches along the frontal slope. (b) Propagating wedge during stable thrusting. (c) Nucleation of frontal thrust in input layer. (d) Frontal accretion and uplift of new thrust ridge. Same experimental phase as shown in Figs. 6 and 7.

The propagation of the basement-controlled normal fault into the overlying sand layer is monitored from initial formation to its final configuration with the 2D incremental displacement vectors and incremental shear strain $E_{yx}$ that image the particle motion and active shear deformation in the sand layer (Fig. 11).

In general, results of this experiment can be compared with earlier experiments with the same boundary conditions (Horsefield, 1977). Initial displacement along the basement fault initiated a 'precursor' fault (Mandl, 2000) in accordance with the stress field above a rigid basement fault. In the PIV images, this zone of localized deformation is visible much earlier than in the raw images, clearly showing that the template of future shear zones is established before these become visible by conventional visual inspection.

With progressive displacement of the basement fault, the fault migrates through the material into a kinematically favourable position. The 'far field' displacement field is, as expected parallel to the displacement vector of the moving basement block, whereas the material above the fixed basement block only moved initially during elastic deformation (Fig. 11B). Initial displacement in the sand layers was accommodated by a distributed triangle-shaped deformation zone with localized deformation above the step in the basement. The geometry and kinematics of this deformation zone is comparable with a releasing bend with respect to the kinematics of the basement fault.

The right boundary of the deformation zone, located subvertically above the basement step, separates deformed material from footwall material at rest. The left boundary, dipping antithetically to the basement fault, marks the transition between deformed material and the undeformed hanging wall material.

In contrast to the tectonic compression experiments and the ring shear test under normal load described in this paper, there is almost no compaction of the material in the tectonic extension experiments before strain localization and decompaction.

Shear zone migration itself is a discontinuous process, presumably because of the non-linear interaction between pre-failure strain hardening and softening during decompaction of the sand. The active shear zone remained active until peak strength of the decompacting material on the right side was reached. Subsequently, strain localization and transfer of straining into the kinematically more favourable new shear zone segment occurred relatively fast, and involved the formation of lens-shaped bodies surrounded by shear zones. The final kinematically stable and steeply dipping linear shear zone was reached by two subsequent migration phases of the deformation band during the experiment (Fig. 11c–d and e–f). The reason for this discontinuous lateral migration of the shear zone is not well understood. The finite strain pattern is that of a complex shear zone in which the fault segments became progressively younger towards the footwall.

## 6. Discussion and outlook

On the meso-scale, upper crustal faults have a very complex strain history with variable strain pattern and strong strain gradients. This complexity results from contrasting modes of strain accumulation with distributed and localised deformation. These contrasting deformation processes interact on various spatial and temporal scales and are directly coupled to the non-linear strain-dependent material strength of brittle rocks. This complex deformation behaviour can be simulated by physical granular-flow experiments (Dahlen and Suppe, 1988; Lallemand et al., 1994; McClay, 1996; Koyi, 1997; Schellart, 2000; Lohrmann et al., 2003). However, their quantitative analysis was restricted by the resolution of strain data obtained by time-consuming conventional analysis techniques.

For high-resolution strain monitoring, we applied optical image correlation techniques (*p*article *i*maging *v*elocimetry). To demonstrate the potential of analogue experiments in combination with PIV, we monitored the spatial and temporal pattern of strain accumulation during shear zone formation in mechanically homogeneous contractional and extensional sandbox experiments. The examples of 2D and 3D displacement data show that the high-resolution PIV is a highly versatile, practical tool which allows quantification of all strain components in the experiments on a routine basis, including both distributed strain as well as localised strain with its strong gradients.

### 6.1. Strain accumulation in sandbox experiments

Our experimental results show that in addition to the external boundary conditions the mode, pattern, and temporal variation of strain accumulation are also controlled by the strain-dependent strength of the granular material (Fig. 9). On a local scale, the deformation behaviour depends on the actual strain level stored in the particular material volume, here referred to as 'local strain memory' (Fig. 8). At low strain levels ($E_{xy}<0.1$), strain is locally accumulated by distributed deformation that indicates pre-failure strain hardening. Spontaneous shear localisation starts in local material volumes where the threshold strain level is achieved to overcome peak strength ($E_{xy}\sim0.1$). With further increasing strain levels, continuous shear localisation is maintained by strain softening until stable shear conditions are established ($E_{xy}>0.2$).

The variable material flux in the sandbox experiments causes strong local strain variability and an inhomogeneous strain memory. Thus, the related deformation mechanism and pattern of strain accumulation show a rather complex history as imaged in the experiments by time-series data. In the shear zone/fault initiation stage, localisation and early

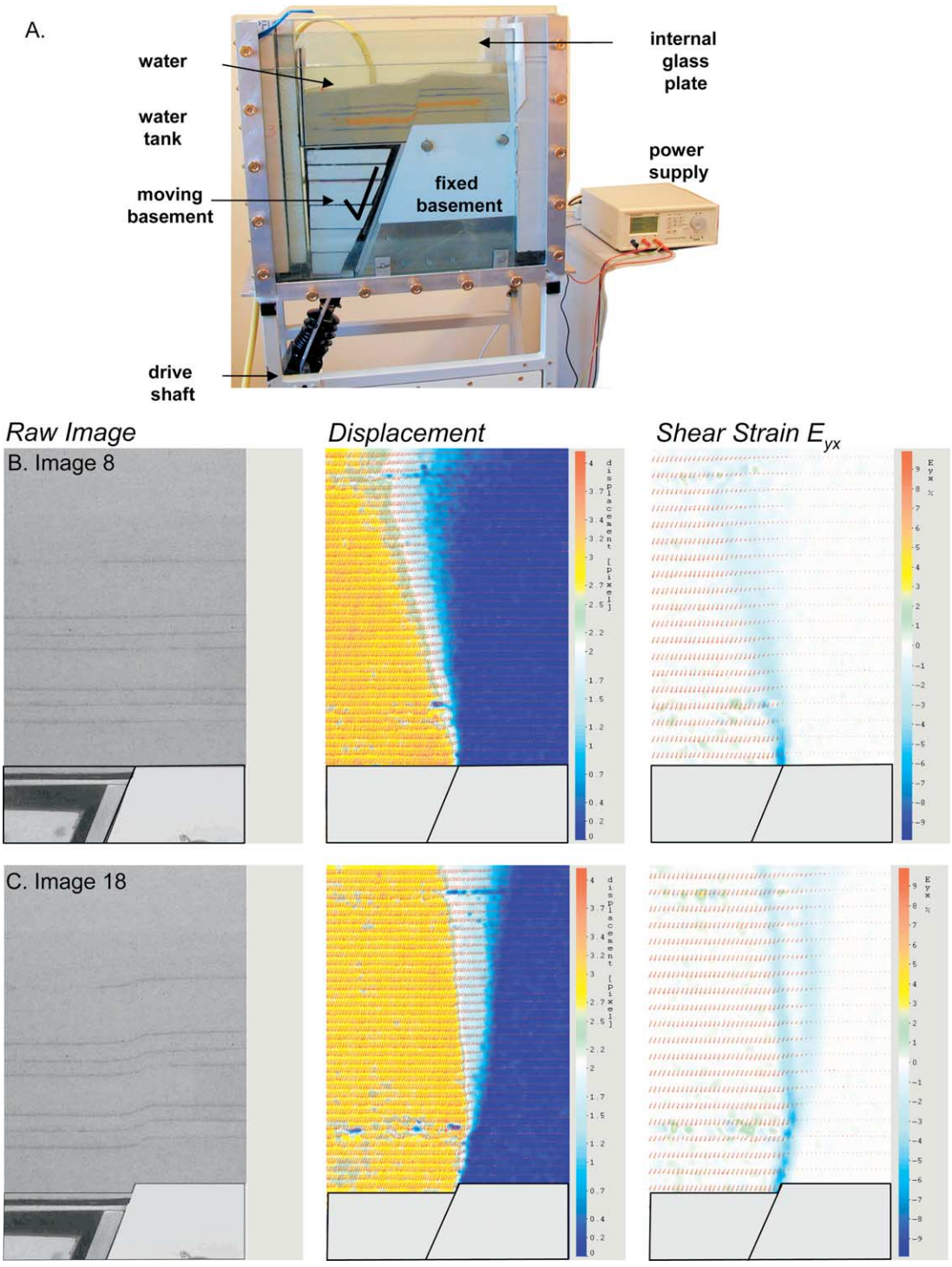


Fig. 11. Discontinuous strain accumulation and fault propagation in the extensional wet sandbox experiment: (A) Experimental setup. (B)–(F) Characteristic stages of shear zone evolution. Raw images (left column), incremental 2D displacement field data shown as vector presentation with vector length (centre column) and with strain $E_{yx}$ (right column) as background colour map. Local heterogeneities in the vector field are due to noise from conversion of colour image data or artefacts from image compression.

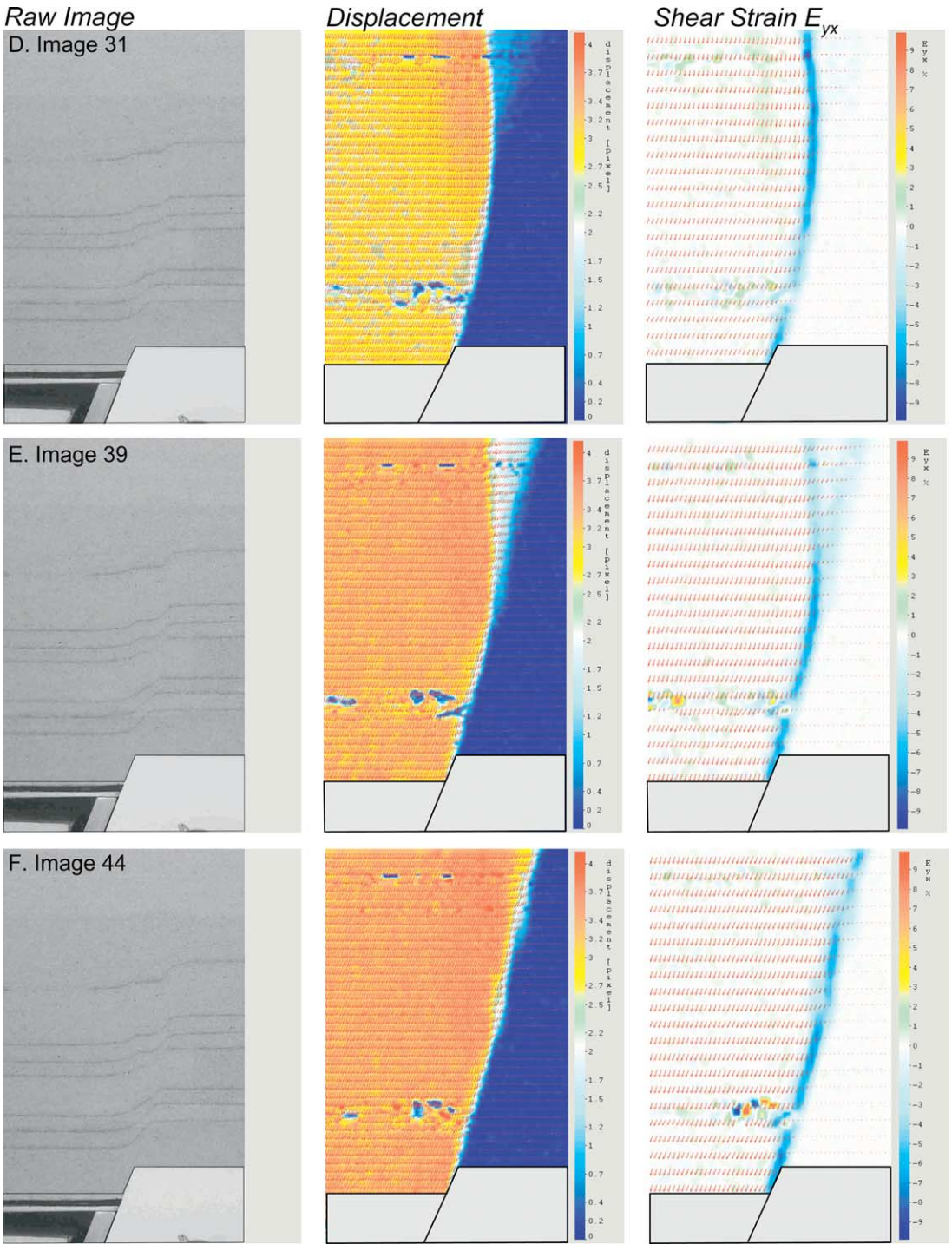


Fig. 11 (*continued*)

Table 3
Specifics and database of the extensional wet sandbox experiment

| 2D wet sandbox experiment—basement-controlled normal fault | |
|---|---|
| Scaling factor | $10^5$ |
| Initial setup | Poured sand layer, 150 mm thick on rigid basement, submerged |
| Sand | 0.1–0.4 mm |
| Basement fault | Fixed FW block, movable HW driven by electric motor, fault dip = 70° |
| Maximum vertical displacement | 60 mm |
| Displacement rate | 0.67 mm/min |
| Duration | 67 min |
| PIV frame rate | 0.033 Hz, $dt = 30$ s |
| PIV raw data | 133 images |

structural development of the shear zone is controlled by distributed deformation with strain hardening. Active shear zones discontinuously develop towards a mechanically favoured orientation by distributed strain propagation into the host material followed by episodic fault re-location after local peak strength is exceeded.

### 6.2. Comparison with natural deformation

Related patterns of strain accumulation and localisation during brittle deformation are observable in natural systems. Similar deformation processes and mechanisms as monitored during shear zone formation in front of the propagating sand wedge were studied in detail in ODP cores and seismic data from the deformation front of accretionary prisms. Here, a significant amount of tectonic strain is accumulated by distributed deformation during frontal accretion of trench sediments and is indicated by tectonic thickening and porosity reduction in the undeformed sediments several kilometres in front of the accretionary wedge (Morgan and Karig, 1995; Adam et al., 2004). In this tectonic setting, distributed deformation is attributed to pervasive small-scale brittle deformation by micro-faulting and the formation of deformation bands (Maltman, 1984; Karig and Lundberg, 1990; Taira et al., 1992) and tectonic porosity reduction in arcward direction (Bray and Karig, 1988; Taira et al., 1992). A similar genesis is described for the propagation of crustal faults, e.g. blind thrusts at the deformation front of thrust belts, where the tip of the propagating fault is characterised by a region with penetrative minor faulting or micro-cracking with gradually decreasing fault displacement (Atkinson, 1987; Jamison, 1993).

### 6.3. Advances in physical simulation of brittle rock deformation

Optical strain monitoring (PIV) in sandbox experiments bridges the gap from physical modelling to numerical simulation because the quantitative results can be directly correlated. Thus, the displacement data of the physical experiments may be used to calibrate and test numerical algorithms and their relevant mechanical parameters for simulating model deformation on different spatial and temporal scales or both methods may be combined to model different aspects of the same model deformation system.

3D-PIV analysis of surface deformation and surface mass transfer can be used to monitor landslides, slope instabilities and surface mass transfer in tectonically active settings. The combination of 2D- and 3D-PIV allows monitoring coupled subsurface–surface deformation processes. Finally, with the high temporal resolution given by monitoring with PIV CCD cameras, it is possible to monitor unstable shear processes and stick-slip deformation processes. Experiments with contemporaneous strain and stress monitoring by additional in-situ stress monitoring (Nieuwland et al., 2000b) will directly link the stress and strain evolution in the experiments.

In the near future, the quantitative results enable detailed material tests to characterise the deformation behaviour of analogue materials and to analyse their additional scaling properties as work hardening or elasticity and their relevance for different experimental objectives.

## Acknowledgements

This study was financially supported by the Deutsche Forschungsgemeinschaft (Leibniz programme, On7/10-1). Technical assistance in the GFZ analogue modelling laboratory came from Günter Tauscher. Invaluable assistance by Karl Nienhaus (BGRM, RWTH) with design and construction of the underwater sandbox apparatus is gratefully acknowledged. We gratefully thank G. Schreurs and D.A. Nieuwland for helpful reviews of this manuscript.

## Appendix A. Basic steps of 2D displacement vector calculation with optical image correlation

Fig. 2 illustrates the basic steps of cross-correlation and computation of the 2D displacement field from two successive images (image 1 at time ($t$) and image 2 at

time ($t+dt$)). The images are divided into small sub-samples (interrogation windows IW 1 and IW 2, Fig. 2A and B at position ($n$, $m$)). The second interrogation window is shifted incrementally by ($dx$, $dy$) in the $x$- and $y$-directions and pattern correlation is calculated by fast Fourier transformation (correlation map). The maximum correlation peak is the most likely local displacement vector ($dx$, $dy$) for this sub-sample to match the pattern of the IW 1 to IW 2 (Fig. 2C). This digital cross-correlation yields a spatial average of the local displacement vector over the size of the sub-sample without the need to track single particles. The complete displacement field consists of all vectors ($n$, $m$) of all interrogation windows for the field of view (Fig. 2D).

A higher validation rate is achieved with iterative vector calculation steps with intermediate vector post-processing. Higher spatial resolution is reached by adaptive multi-pass correlation (Fincham and Spedding, 1997; Scarano and Riethmuller, 2000; Wieneke, 2001) and a step-wise decreasing of the sub-sample size from one iteration to the next (Fig. 2E). The displacement vector ($n$, $m$) calculated from the previous (multi) pass is used as IW pre-shift for the current pass as best estimation for the most probable movement. In this way large deformations can be detected with small IW sizes, which increase spatial resolution.

These displacement field data are now the basis for further information as scalar fields describing the local movement in $x$ or $y$, velocity or derived values as the strain tensor components $E_{ij} = dV_{i'}(x)/dx_j$ ($i$, $j = 1\ldots3$), which describe the change of vector components along the axis 1…3 (Fig. 6). Further values can be derived from these as the rotational shear $rot\text{-}z = E_{yx} - E_{xy}$ the Poisson ratio $\nu = -E_{xx}/E_{yy}$ or the shear strength (complex part of the eigenvalues of the strain tensor).

## Appendix B. 3D displacement vector calculation of deforming free surfaces

The measurement of the 3D displacement of free deforming surfaces with PIV is achieved by correlation of images obtained by a stereoscopic camera setup (Fig. 3a). The 3D procedure consists of three steps with: (1) 3D volume calibration, (2) static measurement of the surface shape, and (3) dynamic measurement of 3D surface deformation and 3D displacement of surface elements.

(1) 3D volume calibration provides a mapping function $M'$ for image correction for the given experiment volume. For this purpose, equidistant stereo images of a calibration plate with equidistant cross marks are recorded that cover the entire experiment volume. For each vertical section starting at 0 cm over the total depth $d$, the stereo cameras are synchronously levelled stepwise by translation stages (Fig. 3) at the respective vertical camera positions and a stereo image of the calibration plate is recorded. From the parallax offset of the marks at different levels the mapping function $M'$ (3rd order polynomial) of the respective camera setup is calculated. With $M'$ the surface height $H(x, y)$ at position ($x$, $y$) is calculated by the offset of particles in the stereo images at time $t$ (static measurement).

(2) For each stereo image (Fig. 4) at time ($t$, $t+dt$, $t+2dt$, etc.), surface height calculation with $M'$ provides a scalar field describing the actual surface of the object $S(x, y, H(x, y))_{t+ndt}$ that is a prerequisite for 3D displacement calculation (Fig. 4b). By PIV correlation methods the virtual shift (parallax offset) of identical surface elements (patterns) is calculated. For each image location the corresponding surface height can be calculated from the virtual shift with the mapping function $M'$.

(3) 3D displacement calculation leads to a vector field describing the displacement of every surface point. The 3D surface displacement $V(x, y, H(x, y))$ is calculated by cross-correlation from successive stereo images ($t(t+dt)$) in the same way as described for 2D PIV with $V(x, y, H=0)$. With the surface height information and the mapping function $M'$, for each vector position ($x$, $y$) the 2D displacement vector is calculated for both stereo cameras separately (Fig. 4c). Finally, the 3D displacement vector $V(x, y, H(x, y))$ is calculated from the two 2D displacements of both images together with the corresponding surface height (Fig. 4e).

## Appendix C. Precision of PIV correlation

For a given experiment the absolute spatial resolution of the displacement field data depends on the optical resolution of the digital camera system and the precision of the cross-correlation algorithm.

Image data from digital still cameras of the consumer segment with 4 mega-pixels resolution (RGB) are sufficient for PIV analysis (for example, extensional wet sandbox experiment) but have some drawbacks. First of all the maximum repetition rate is often 0.1 Hz or less and they cannot be triggered electronically although this may be not necessary for certain experiments. Furthermore, the pixels are masked by red, green and blue filters and the resulting 'coloured pixels' are downmixed from intensity information of neighbour colour pixels. So the effective spatial resolution is only 2/3 of a monochrome camera. Therefore, coloured particles leave a non-uniform intensity path when moving across the pixels. Because the PIV algorithm uses a correlation algorithm for scalar intensity values, a 'mono-monochrome' scalar intensity must be derived from the colour pixel information and there are many different colour space models to do this. Last but not least, consumer cameras often allow storage of only compressed and lossy JPG images, which contain artefacts that influence the

correlation algorithm and hence lower the PIV correlation accuracy. Digital motion-picture CCD cameras (for example FlowMaster 2S 4 mega-pixels, monochrome) optimised for PIV monitoring allow image acquisition with full optical resolution and without loss of intensity information by image conversion and compression. Digital CCD cameras achieve constant frame transfer rates of maximum 15 Hz without image compression and no loss of image information.

As demonstrated by White et al. (2001), PIV cross-correlation algorithms allow the calculation of displacement vectors in sand with sub-pixel accuracy ($<0.1$ pixel). For the adaptive multi-pass cross-correlation algorithm of the StrainMaster© PIV system (LaVision GmbH, 2002), used in the adapted system of this study, the accuracy of the vectors is on average significantly smaller than 0.1 pixel and ranges from 0.03 to 0.2 pixel depending on the size of the interrogation window and image contrast (LaVision, 2002). Derived values as strain components have a relative error of 0.3–1.25% depending on the interrogation window size and overlap. With a given optical vector accuracy of better than 0.1 pixel, the absolute accuracy of the displacement vectors ($dx$) depends on image scaling and correction. For example, with an optical resolution of 4 mega-pixels ($2k \times 2k$) and an experiment with 100 cm width $dx$ is about 0.1–0.05 mm.

## References


Adam, J., Lohrmann, J., Hoth, S., Kukowski, N., Oncken, O., 2002. Strain variation and partitioning in thrust wedges: high-resolution data from scaled sandbox experiments by 2D–3D PIV analysis. Bollettino di Geofisica teorica ed applicata 42 (1/2), 123–126.

Adam, J., Klaeschen, D., Kukowski, N., Flueh, E.H.R., 2004. Upward delamination of Cascadia Basin sediment infill with landward frontal accretion thrusting caused by rapid glacial age material flux. Tectonics, 23(3), TC3009, doi:10.1029/2002TC001475.

Atkinson, B.K., 1987. Introduction to Fracture Mechanics and its Geophysical Applications. Academic Press, London, UK.

Bray, J.C., Karig, D.E., 1988. Dewatering and extensional deformation of the Shikoku Basin hemipelagic sediments in the Nankai Trough. Pure & Applied Geophysics 128, 725–747.

Dahlen, F.A., Suppe, J., 1988. Mechanics, growth, and erosion of mountain belts. Processes in continental lithospheric deformation. Geological Society of America Special Paper 218, 161–178.

Fincham, A.M., Spedding, G.R., 1997. Low cost high resolution DPIV for measurement of turbulent fluids. Experiments in Fluids 23, 449–462.

Gutscher, M.A., Kukowski, N., Malavieille, J., Lallemand, S., 1996. Cyclical behavior of thrust wedges; insights from high basal friction sandbox experiments. Geology (Boulder) 24 (2), 135–138.

Gutscher, M.A., Kukowski, N., Malavieille, J., Lallemand, S., 1998. Material transfer in accretionary wedges from analysis of a systematic series of analog experiments. Journal of Structural Geology 20 (4), 407–416.

Horsefield, W.T., 1977. An experimental approach to basement-controlled faulting. Geologie en Mijnbouw 56, 363–370.

Huiqui, L., McClay, K.R., Powell, D., 1992. Physical models of thrust wedges, in: McClay, K.R. (Ed.), Thrust Tectonics. Chapman & Hall, London, UK, pp. 71–81.

Jamison, W.R., 1993. Mechanical stability of the triangle zone: the backthrust wedge. Journal of Geophysical Research 98 (B11), 20015–20030.

Karig, D.E., Lundberg, N., 1990. Deformation bands from the toe of the Nankai accretionary prism. Journal of Geophysical Research 95, 9099–9109.

Koyi, H., 1997. Analogue modelling; from a qualitative to a quantitative technique; a historical outline. Journal of Petroleum Geology 20 (2), 223–238.

Kukowski, N., Lallemand, S.E., Malavieille, J., Gutscher, M.A., Reston, T.J., 2002. Mechanical decoupling and basal duplex formation observed in sandbox experiments with application to the Western Mediterranean Ridge accretionary complex. Marine Geology 3068, 1–13.

Lallemand, S.E., Schnuerle, P., Malavieille, J., 1994. Coulomb theory applied to accretionary and nonaccretionary wedges; possible causes for tectonic erosion and/or frontal accretion. Journal of Geophysical Research B, Solid Earth and Planets 99 (6), 12,033–12,055.

LaVision, 2002.Anon., 2002. StrainMaster Manual for DaVis 6.2. LaVision GmbH, Goettingen.

Lohrmann, J., Kukowski, N., Adam, J., Oncken, O., 2003. The impact of analogue material parameters on the geometry, kinematics, and dynamics of convergent sand wedges. Journal of Structural Geology 25 (10), 1691–1711.

Maltman, A., 1984. On the term 'soft-sediment deformation'. Journal of Structural Geology 6, 589–592.

Mandl, G., 1988. Mechanics of Tectonic Faulting: Models and Basic Concepts. Elsevier, New York.

Mandl, G., 2000. Faulting in Brittle Rocks; an Introduction to the Mechanics of Tectonic Faults. Springer, Berlin, Germany. 434pp.

Marchner, T., Vermeer, P.A., 2001. Macromodelling of softening in non-cohesive soils, in: Vermeer, P.A., Diebels, S., Ehlers, W., Herrman, H.J., Luding, S., Ramm, E. (Eds.), Continuous and Discontinuous Modelling of Cohesive-Frictional Materials. Springer, Berlin, Heidelberg, New York, pp. 88–110.

Marone, C., 1998. Laboratory-derived friction laws and their application to seismic faulting. Annual Reviews of Earth and Planetary Science 26, 643–696.

McClay, K.R., 1996. Recent advances in analogue modelling: uses in section interpretation and validation, in: Buchanan, P.G., Nieuwland, D.A. (Eds.), Modern Developments in Structural Interpretation, Validation and Modelling Geological Society Special Publication, 99, pp. 201–225.

McClay, K.R., Ellis, P.G., 1987. Analogue models of extensional fault geometries, in: Coward, M.P., Dewey, J.F., Hancock, P.L. (Eds.), Continental Extensional Tectonics Special Publication of the Geological Society, London, 28, pp. 109–125.

Morgan, J.K., Karig, D.E., 1995. Kinematics and a balanced and restored cross-section across the toe of the eastern Nankai accretionary prism. Journal of Structural Geology 17 (1), 31–45.

Nieuwland, D.A., Leutscher, J.H., Gast, J., 2000a. Wedge equilibrium in fold-thrust belts: prediction of out-of sequence thrusting base on sandbox experiments and natural examples. Geologie en Mijnbouw/-Netherands Journal of Geoscience 79 (1), 81–91.

Nieuwland, D.A., Urai, J.L., Knoop, M., 2000b. In-situ stress measurements in model experiments of tectonic faulting, in: Lehner, F.K., Urai, J.L. (Eds.), Aspects of Tectonic Faulting. Springer, Berlin, Germany, pp. 155–166.

Scarano, F., Riethmuller, M.L., 2000. Advances in iterative multigrid PIV image processing. Experiments in Fluids (Suppl.) 29, 51–60.

Schellart, W.P., 2000. Shear test results for cohesion and friction coefficients for different granular materials; scaling implications for their usage in analogue modelling. Tectonophysics 324 (1-2), 1–16.

Schmatz, J., van der Zee, W., Urai, J.L., 2003. Fault Gouge Evolution in

Layered Sand-Clay Sequences—First Results of Water-Saturated Sandbox Experiments. In: EAGE Conference on Fault and Top Seals, O22.

Taira, A., Hill, I., Firth, J.V., Berner, U., Brueckmann, W., Byrne, T., Chabernaud, T., Fisher, A., Foucher, J.P., Gamo, T., Gieskes, J.M., Hyndman, R.D., Karig, D., Kastner, M., Kato, Y., Lallemant, S., Lu, R., Maltman, A.J., Moore, G., Moran, K., Olaffson, G., Owens, W., Pickering, K., Siena, F., Taylor, E., Underwood, M., Wilkinson, C., Yamano, M., Zhang, J., 1992. Sediment deformation and hydrogeology of the Nankai Trough accretionary prism; synthesis of shipboard results of ODP Leg 131, in: Kastner, M., Le, P.X. (Eds.), Fluids in Convergent Margins Earth and Planetary Science Letters, 109. Elsevier, Amsterdam, Netherlands, pp. 431–450.

Wang, W.H., Davis, D., 1996. Sandbox model simulation of forearc evolution and noncritical wedges. Journal of Geophysical Research B, Solid Earth and Planets 101 (5), 11,329–11,339.

White, D.J., Take, W.A., Bolton, M.D., 2001. Measuring soil deformation in geotechnical models using digital images and PIV analysis. In: 10th International Conference on Computer Methods and Advances in Geomechanics, Tucson, Arizona.

Wieneke, B., 2001. PIV adaptive multi-pass correlation with deformed interrogation windows. PIV Challenge 2001; 1–6.

Wolf, H., König, D., Triantafyllidis, T., 2003. Experimental investigation of shear band patterns in granular material. Journal of Structural Geology 25, 1229–1240.

van der Zee, W., 2002. Dynamics of Fault Gouge Development in Layered Sand–Clay Sequences. Shaker Verlag, Aachen.

van der Zee, W., Urai, J., Richard, P., 2003. Lateral clay injection into normal faults. GeoArabia 8 (3), 501–522.